PHYSICAL REVIEW A VOLUME 49, NUMBER 4 APRIL 1994

# Spatial properties of spontaneous parametric down-conversion and their effect on induced coherence without induced emission

T. P. Grayson and G. A. Barbosa*
*Department of Physics and Astronomy, University of Rochester, Rochester, New York 14627*

(Received 1 September 1993)

The quantum state for spontaneous parametric down-conversion was evaluated to include information about the transverse spatial characteristic of the down-conversion fields. This state was used to calculate the angular spectrum of down-conversion in the case of both single-channel and coincidence measurements, while retaining the characteristic nonclassical correlations. Actual transverse profiles for typical experimental parameters were evaluated numerically and measurements were performed with results that compared well with the numerical calculation. This theoretical spatial model was then applied nonrigorously to the case of induced coherence without induced emission. The theoretical results implied that there was a reduction in the degree of induced coherence due strictly to the spatial distribution of the down-conversion beams. This was interpreted as a result of increased distinguishability of the overlapping idler photons. Measurements were conducted which support these results qualitatively. In addition, the present theory explained an unexpected quantitative discrepancy between second- and fourth-order visibilities in previous induced-coherence experiments. This descrepancy was interpreted phenomenologically as a difference between intrinsic and nonintrinsic indistinguishability, and some implications towards quantum measurement theory and the role of the observer were suggested.

PACS number(s): 42.65.Ky, 42.50.Dv

## I. INTRODUCTION

The process of spontaneous parametric down-conversion has been utilized in many experiments in recent years [1–10]. As is well known, this process involves the "conversion" of a pump photon of a given frequency into two photons of lower frequencies, called the signal and idler photons for historical reasons, such that energy is conserved. Down-conversion has been paricularly useful as a light source for tests of fundamental quantum mechanics, because the signal and idler photons are produced as a highly correlated pair [1–10].

Despite the usefulness of this process, not much is known about the spatial properties of the down-converted light. The spatial distribution of down-converted light is governed by the process of phase matching, the assertion that the wave vectors of the down-converted light added vectorially must equal the wave vector of the pump light. This is equivalent to conservation of momentum. However, as we shall see, this is a weak condition, and the real situation is slightly more complicated. There have been numerous treatments of phase matching and the spatial distribution of classical nonlinear optical processes, including the classical analog of down-conversion, parametric amplification [11–13], and at least one recent quantum mechanical treatment of down-conversion allows the possibility of a spatial analysis [14]. The classical treatment, however, loses the photon correlation information that is crucial to the above-mentioned nonclassical experiments, and the quantum treatment above was limited to one dimension, the direction of propagation, because of the complexity of the calculation. There is yet another new quantum mechanical approach by Koch *et al.* [15] which addresses the transverse properties using quantum scattering theory, but again does not treat the correlations.

In the first half of the paper this problem of the spatial distribution of spontaneous down-conversion will be examined in detail. The analysis will begin with the quantum state for down-converted light in the interaction picture derived by Wang *et al.* [16,17]. This formulation contains information about phase matching conditions and the spatial distribution of the down-conversion, but to simplify calculations, Wang *et al.* treated an idealized case in which the pump beam and the down-conversion beams are perfectly collimated and aligned exactly at phase-matching angles. These assumptions are not made here, so that an angular spectrum of the down-conversion may be calculated. The spectrum for one set of realistic parameters is calculated numerically. The results are then confirmed experimentally.

The second half of the paper addresses the effect of finite spatial extent on the process known as induced coherence without induced emission [17], in which coherence is induced between the signal beams of two coherently pumped down-converter crystals by carefully aligning the idler beams of the two down-converters to overlap exactly. The resulting coherence was interpreted as a manifestation of the indistinguishability of the two signal

---

*Permanent address: Departamento de Física ICEx, Universidade Federal de Minas Gerais, CP 702, Belo Horizonte 31261 MG, Brazil.

1050-2947/94/49(4)/2948(14)/$06.00

paths when the corresponding idlers are made indistinguishable by the alignment [17]. Indeed, it was shown by Mandel that the probability that two paths are indistinguishable is equal to the degree of coherence for two interfering beams of light [18]. While the basic principle of induced coherence without induced emission was demonstrated experimentally by Zou *et al.* [6], the visibilities measured in the experiment were significantly less then the theoretically predicted values. In addition there was a significant discrepancy between the measured second- and fourth-order visibilities that was not predicted by theory.

This paper addresses the effect of the transverse spatial distribution of the down-conversion on the induced-coherence process. It is conjectured that the spatial extent of the down-conversion beams causes the overlapping idler beams to be partially distinguishable, even for perfect alignment. A nonrigorous calculation, based on the quantum state of Wang *et al.* [17], supports this conjecture, and experimental data are presented which, at least qualitatively, provide support for this hypothesis.

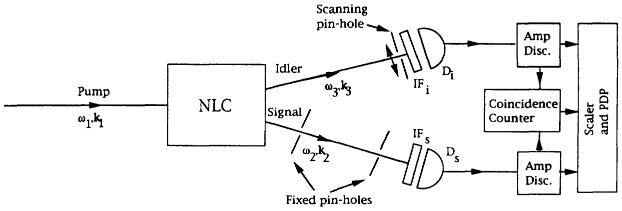

FIG. 1. The experimental setup to produce spontaneous parametric down-conversion. NLC denotes a nonlinear crystal. $IF_i$ and $IF_s$ are 1 nm bandwidth interference filters centered at the down-conversion wavelengths. PDP is a PDP 11/23 computer.

## II. SPATIAL PROPERTIES OF SPONTANEOUS DOWN-CONVERSION

### A. Theory

Before we describe any details of the down-conversion process, it is perhaps helpful to have first an intuitive feel for the sources of down-conversion divergence. First as we shall see, phase matching conditions are not exact, since they are diffractive in nature. As the crystal length decreases, the phase-matching conditions become more relaxed. In addition even for perfect phase-matching, if we are to detect a finite bandwidth of frequencies, each has a corresponding wave vector with a slightly different direction of propagation. Finally if the pump beam is not perfectly collimated, each wave vector in its spread has a corresponding spread of down-conversion wave vectors associated with it. Below it is shown how these ideas may be introduced into the down-conversion theory.

An experimental setup to produce down-conversion is shown in Fig. 1. A pump beam of frequency $\omega_1$ and wave vector $\mathbf{k}_1$ is directed into an optically active crystal with second-order nonlinear susceptibility $\chi^{(2)}$, producing down-conversion signal and idler beams $s$ and $i$ with frequencies $\omega_2$ and $\omega_3$ and wave vectors $\mathbf{k}_2$ and $\mathbf{k}_3$, respectively. In Refs. [16,17] Wang *et al.* have found the quantum state of spontaneous down-conversion in the interaction picture to a first-order approximation to be

$$|\psi(t)\rangle = |\text{vac}\rangle_{s,i} + \eta\frac{\delta\omega^{3/2}}{2\pi^{1/2}}\sum_{\omega_1}\sum_{\omega_2}\sum_{\omega_3}\phi(\omega_2,\omega_3;\omega_1)\frac{\sin\Omega t_1/2}{\Omega/2}\,\exp^{i\Omega(t-t_1/2)}\exp^{-i(\mathbf{k}_2+\mathbf{k}_3-\mathbf{k}_1)\cdot\mathbf{r}_0}\,v(\omega_1)|\omega_2\rangle_s|\omega_3\rangle_i. \quad (1)$$

Here $v(\omega)$ is the classical field amplitude of the pump, $t_1$ is the interaction time of the pump field with the crystal, $\Omega = \omega_2+\omega_3-\omega_1$, $\mathbf{r}_0$ is the position of the center of the crystal, $\eta$ is a coefficient containing the nonlinear susceptibility, and $\phi(\omega_2,\omega_3;\omega_1)$ represents the spectrum of the down-conversion. It is the function $\phi$ that needs to be examined in more detail.

The $\phi(\omega_2,\omega_3;\omega_1)$ function is defined in the reference as [16,17]

$$\phi(\omega_2,\omega_3;\omega_1) \equiv M\prod_{m=1}^{3}\left(\frac{\omega_m}{\omega_{m0}}\right)^{1/2}\frac{\sin(\mathbf{k}_2+\mathbf{k}_3-\mathbf{k}_1)_m l_m/2}{(\mathbf{k}_2+\mathbf{k}_3-\mathbf{k}_1)_m/2}, \quad (2)$$

where $\omega_{m0}$ is the center frequency of field $m$, $l_m$ is the length of the interaction volume in the $m$ direction, and $(\mathbf{k}_2+\mathbf{k}_3-\mathbf{k}_1)_m$ is the $m$th component of $\mathbf{k}_2+\mathbf{k}_3-\mathbf{k}_1$. $M$ is a normalization constant such that

$$2\pi\delta\omega\sum_{\omega}|\phi(\omega_{20}+\omega,\omega_{30}-\omega;\omega_{10})|^2 = 1. \quad (3)$$

If the down-converted beams are assumed to be collimated with fixed propagation directions, then the directions of the wave vectors are constants and only the magnitudes vary, thereby justifying a summation only over frequency as in Eq. (1). This need not be the case, however, in a realistic system, since diverging beams and finite dimension pinholes define a range of possible direction within the accuracy of phase matching. It is therefore necessary to take into account variation in direction as well as frequency.

The geometry of the down-conversion process may be represented by Fig. 2. The center of the pump beam propagation is considered to be the $z$ axis, although if it is divergent, it can be composed of a spread of wave

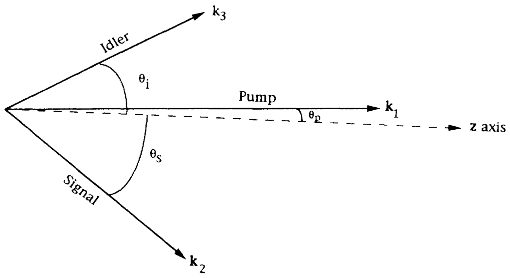

FIG. 2. A schematic representation of the geometry of parametric down-conversion demonstrating phase matching. The $z$ axis of the laboratory coordinate system is as shown. The $x$ axis is in the plane of the page, and the $y$ axis is perpendicular to the page.

vectors at small angles $\theta_1$ about the $z$ axis . The down-conversion fields are considered to be confined in the $x$-$z$ plane at angles $\theta_2$ and $\theta_3$ to the $z$ axis, and the optic axis of the crystal is confined in the $y$-$z$ plane at an angle $\varphi$ to the $z$ axis. The down-conversion profile could be extended to three dimensions in a straightforward manner, but it is treated here in two dimensions for simplicity. The phase matching is considered to be type I, with the pump field chosen to be the $e$ wave, polarized in the $y$ direction, and the down-conversion fields as $o$ waves, polarized approximately in the $x$ direction.

The magnitude of the wave vectors is given by

$$k_m = \frac{\omega_m n_m(\omega_m)}{c}, \tag{4}$$

where $n_m(\omega_m)$ is the refractive index at frequency $\omega_m$. The two down-conversion beams have indices $n_o(\omega_2)$ and $n_o(\omega_3)$, where $n_o(\omega)$ is the ordinary index of refraction of the crystal at frequency $\omega$. Since the pump is an extraordinary wave with its propagation at some angle $\varphi$ to the optical axis of the crystal, its effective index of refraction takes the form [19]

$$n_{e3}(\omega_1) = \left[\frac{\cos^2\varphi}{n_o^2(\omega_1)} + \frac{\sin^2\varphi}{n_e^2(\omega_1)}\right]^{-1/2}, \tag{5}$$

where $n_e(\omega)$ is the extraordinary index of refraction of the crystal at frequency $\omega$.

Using the geometry shown in Fig. 2 along with Eq. (4), Eq. (2) becomes

$$\phi(\omega_2,\omega_3;\omega_1|\theta_2,\theta_3;\theta_1) = M\left[\prod_{m=1}^{3}\left(\frac{\omega_m}{\omega_{m0}}\right)^{1/2}\right]\frac{\sin[\omega_2 n_o(\omega_2)\cos(\theta_2)+\omega_3 n_o(\omega_3)\cos(\theta_3)-\omega_1 n_{e3}\cos(\theta_1)]l_{\mathbf{z}}/2c}{[\omega_2 n_o(\omega_2)\cos(\theta_2)+\omega_3 n_o(\omega_3)\cos(\theta_3)-\omega_1 n_{e3}\cos(\theta_1)]/2c}$$
$$\times\frac{\sin[\omega_2 n_o(\omega_2)\sin(\theta_2)-\omega_3 n_o(\omega_3)\sin(\theta_3)-\omega_1 n_{e3}\sin(\theta_1)]l_{\mathbf{x}}/2c}{[\omega_2 n_o(\omega_2)\sin(\theta_2)-\omega_3 n_o(\omega_3)\sin(\theta_3)-\omega_1 n_{e3}\sin(\theta_1)]/2c}. \tag{6}$$

$\theta_1$ is zero for a collimated pump laser. Rather than being normalized the condition on $\phi$ in Eq. (3) now becomes

$$2\pi\delta\omega\sum_{\omega}|\phi(\omega_{20}+\omega,\omega_{30}-\omega;\omega_{10}|\theta_2,\theta_3;\theta_1)|^2 = G(\theta_2,\theta_3;\theta_1), \tag{7}$$

where $G(\theta_2,\theta_3;\theta_1)$ may now be considered as an angular spectrum for the down-conversion.

The detection process will be treated in more detail in a later section, but for now the results of previous calculations in Ref. [17] will be quoted without proof. If we refer to the experiment pictured in Fig. 1, the intensity of either the signal or idler beam, as given in terms of a counting rate for the respective photon-counting detector, is given by [16,17]

$$R_s = \alpha_s|\eta|^2\langle I\rangle, \tag{8}$$

$$R_i = \alpha_i|\eta|^2\langle I\rangle, \tag{9}$$

where $\alpha_s$ and $\alpha_i$ are the quantum efficiencies of the signal and idler detectors, respectively, $|\eta|^2$ is the down-conversion efficiency, and $\langle I\rangle$ is the average intensity of the classical pump field. To arrive at this result the normalization given in Eq. (3) was utilized. If the angle-dependent spectral function in Eq. (6) is used instead of the original $\phi$ function, then Eqs. (8) and (9) become

$$R_s(\theta_s) = \alpha_s|\eta|^2\langle I\rangle 2\pi\sum_{\theta_p}g(\theta_p)\sum_{\omega}|\phi(\omega_{s0}+\omega,\omega_{i0}-\omega;\omega_0|\theta_s,\Theta_i(\omega_{s0}+\omega,\omega_{i0}-\omega;\omega_0|\theta_p);\theta_p)|^2, \tag{10}$$

$$R_s(\theta_i) = \alpha_i|\eta|^2\langle I\rangle 2\pi\sum_{\theta_p}g(\theta_p)\sum_{\omega}|\phi(\omega_{s0}+\omega,\omega_{i0}-\omega;\omega_0|\Theta_s(\omega_{s0}+\omega,\omega_{i0}-\omega;\omega_0|\theta_p),\theta_i;\theta_p)|2, \tag{11}$$

where $\omega_{s0}$ is the center frequency of the signal beam, $\omega_{i0}$ is the center frequency of the idler beam, and $\omega_0$ is the pump frequency, assumed to be approximately monochromatic. $\theta_p$ is the angle that the pump wave vector makes with the $z$ axis, and $g(\theta_p)$ is the angular distribution of the pump beam. $g(\theta_p)$ is a $\delta$ function for a collimated beam but is a

Gaussian for a real laser. $\Theta_i(\omega_s,\omega_i;\omega_0|\theta_p)$ is the value of the idler angle that satisfies the phase-matching condition exactly for a given pump angle, and signal, idler, and pump frequencies, and is given by

$$\Theta_i(\omega_s,\omega_i;\omega_0|\theta_p) = \cos^{-1}\left[\frac{n_{e3}^2\omega_0^2 + n_o^2(\omega_i)\omega_i^2 - n_o^2(\omega_s)\omega_s^2}{2n_{e3}n_o(\omega_i)\omega_0\omega_i}\right] - \theta_p. \tag{12}$$

Similarly $\Theta_s(\omega_s,\omega_i;\omega_0|\theta_p)$ is given by

$$\Theta_s(\omega_s,\omega_i;\omega_0|\theta_p) = \cos^{-1}\left[\frac{n_{e3}^2\omega_0^2 + n_o^2(\omega_s)\omega_s^2 - n_o^2(\omega_i)\omega_i^2}{2n_{e3}n_o(\omega_s)\omega_0\omega_s}\right] - \theta_p. \tag{13}$$

This optimal value is used since the status of the undetected field is irrelevant for single-channel detection.

The situation is different for detection of coincidences between signal and idler detectors. The coincidence counting rate calculated in Refs. [16,17] is very similar to the single-channel counting rate

$$R_{s,i} = \alpha_s\alpha_i|\eta|^2\langle I\rangle. \tag{14}$$

For unity quantum efficiency the coincidence rate is identical to the single-channel rates, evidence that signal and idler photons are always produced in coincidence.

If the angle-dependent spectrum of Eq. (6) is used, the coincidence counting rate is now given by

$$R_{s,i}(\theta_s,\theta_i) = \alpha_s\alpha_i|\eta|^2\langle I\rangle \sum_{\theta_p} g(\theta_p) \times \sum_{\omega}\sum_{\omega'} \phi^*(\omega_{s0}+\omega',\omega_{i0}-\omega';\omega_0|\theta_s,\theta_i;\theta_p)\phi(\omega_{s0}+\omega,\omega_{i0}-\omega;\omega_0|\theta_s,\theta_i;\theta_p). \tag{15}$$

Now the detection of the signal influences the angular distribution of the idler and vice versa. This will lead to interesting effects in the induced-coherence experiment that will be discussed later.

### B. Numerical calculations and experimental results

From Eqs. (10) and (15), some spatial distributions may now be calculated for realistic parameters that correspond to the actual experimental setup, and these will be tested experimentally. The system considered is a *lithium iodate* ($\mathrm{LiIO_3}$) second-order nonlinear crystal of dimensions 1 cm×1 cm×2.5 cm. The crystal is pumped by an approximately monochromatic ultraviolet (UV) argon ion laser with a wavelength of 351 nm. The optical axis makes a phase-matching angle of approximately 50.1° with the polarization axis of the pump laser, which is along the $z$ axis of the laboratory coordinates. The idler beam has a center frequency of 633 nm and the signal beam a center frequency of 789 nm, both with a 1 nm bandwidth, defined by two similar interference filters with Gaussian spectra,

$$f_s(\omega) = \exp\left(\frac{-(\omega-\omega_{s0})^2}{2\sigma_{\omega_s}^2}\right),$$

$$f_i(\omega) = \exp\left(\frac{-(\omega-\omega_{i0})^2}{2\sigma_{\omega_i}^2}\right),$$

where $\omega_{s0}$, $\omega_{i0}$, $\sigma_{\omega_s}$, and $\sigma_{\omega_i}$ are the signal and idler center frequencies and the corresponding signal and idler standard deviation bandwidths.

The calculations were performed by evaluating the spectral function of Eq. (6), with the arguments $\phi(\omega_{s0}+\omega,\omega_{i0}-\omega;\omega_0|\theta_s,\theta_i;\theta_p)$, over a frequency range of four standard deviations of the interference filter spectrum. The length $l_z$ is defined as the crystal length of 25.4 mm, and $l_x$ is defined by the pump beam $1/e^2$ half-width, which is approximately 0.9 mm. The indices of refraction were calculated using the Sellmeier formula for $\mathrm{LiIO_3}$ [20]

$$n_o^2 - 1 = \frac{2.401\,09\,\lambda^2}{\lambda^2 - 0.021\,865},$$
$$n_e^2 - 1 = \frac{1.913\,59\,\lambda^2}{\lambda^2 - 0.019\,40}, \tag{16}$$

where $\lambda$ is the wavelength given in $\mu$m. $n_{e3}$ is then given by Eq. (5).

The first calculation is for the case of single-channel detection of the idler beam with an ideal collimated pump beam, so all divergence is due to phase-matching weakness and detection bandwidth. For each value of idler angle $\theta_i$, the spectral function $\phi(\omega_{s0}+\omega,\omega_{i0}-\omega;\omega_0|\Theta_s(\omega_{s0}+\omega,\omega_{i0}-\omega;\omega_0|\theta_p),\theta_i;\theta_p)$ is evaluated with $\theta_p = 0$. $\phi$ is squared, and the result is summed over the full range of $\omega$, with each term weighted by the filter functions $f_s(\omega_{s0}+\omega)$ and $f_i(\omega_{i0}-\omega)$. The results are shown in Fig. 3. As can be seen, the angular spectrum is narrow, corresponding to a beam divergence of about $0.079 \pm 0.002$ mrad.

Next the problem is expanded to include pump beam divergence. The same procedure is performed as above, except that there is an additional sum over pump angles $\theta_p$, where each term is weighted by the angular spectrum of the pump beam,

$$g_p(\theta_p) = \exp\left(\frac{-2\,\theta_p^2}{\Delta\theta_p^2}\right),$$

where $\Delta\theta_p \equiv 0.3$ mrad is the $1/e^2$ divergence angle of the pump beam. The results are shown in Fig. 4. Figure 4(a) is the direct calculation. As can be seen, there is now a good deal of structure. This structure, while inter-

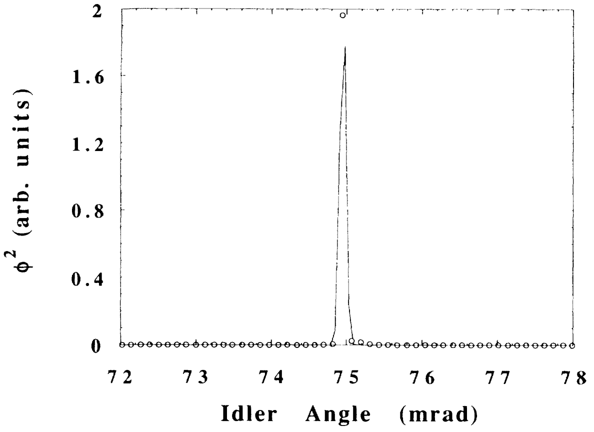

FIG. 3. A numerical calculation of the idler angular spectrum for a single-channel measurement in the case where the pump beam is perfectly collimated. The open circles are the computed data values, and the solid curve is a least squares fit to a Gaussian.

esting, was not investigated further. It is believed to be associated with interference between different off-phase-matching modes that, while very small by themselves, are made more prominent when a divergent pump brings them closer to phase matching. In practice the detector resolution is not fine enough to observe this structure. The finite detection resolution may be simulated by combining a number of neighboring data points to correspond to a more realistic resolution. Figure 4(b) is obtained by grouping every five data points, corresponding to a detector resulution of about 0.6 mrad, or equivalent to a 600 $\mu$m aperture at a distance of 1 m. The limited resolution lends to a smoothing of the structure, producing approximately a Gaussian distribution with a $1/e^2$ width of $0.63 \pm 0.01$ mrad. As can be seen from this result, the divergence is highly dependent on the divergence of the pump beam, enough so as to indicate that the pump divergence is the dominant influence on the down-conversion angular distribution.

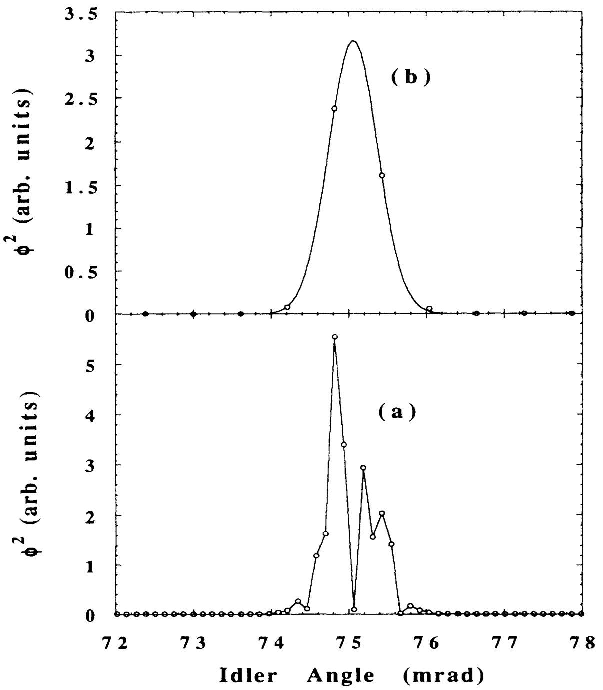

FIG. 4. (a) A numerical calculation of the idler angular spectrum for a single-channel measurement in the case where the pump beam is divergent with a Gaussian profile. (b) The results from (a) smoothed to account for realistic detection resolution. The solid line in (b) is a Gaussian least squares fit, while the solid line in (a) is simply connecting points to excentuate the structure.

Measurements were made to confirm these calculations. The setup is the same as that shown in Fig. 1. The actual experimental parameters are similar to those used in the calculation. The crystal, the interference filters defining the down-conversion beams' spectra, and the pump beam are as in the calculations. The phase-matching angle between the optic axis and the pump polarization is not known exactly; it is adjusted so as to give the best count rate for a given detector position at approximately the expected idler angle, but is in a range between 49.0° and 51.0°.

The measurements are made by placing a photomultiplier tube (PMT), with active aperture much larger than the width of the down-conversion beam, centered on the idler beam at a known distance from the crystal. A pinhole of known diameter is placed in front of the PMT. First, a rough scan is made in the horizontal direction to find the approximate center of the beam. The pinhole is then scanned in steps equal to its diameter, with the count rate of the PMT recorded at each pinhole position, across the vertical extent of the beam. The pinhole is then fixed in the vertical direction at the position that gave the highest count rate, and the scan is repeated in the horizontal direction. The PMT and pinhole are then moved to another distance from the crystal, and the scanning procedure is repeated for several distances from the crystal.

The experimental data are shown in Fig. 5. The results of a sample scan are shown in Fig. 5(a) for a distance of 104 cm from the center of the crystal with a 600 $\mu$m pinhole. The smooth curve is a leasts squares fit to a Gaussian of half-width $1.53 \pm 0.03$ mm. Figure 5(b) shows the $1/e^2$ half-widths of three such scans as a function of distance from the center of the crystal. The solid line is a linear least squares fit with a $1/e^2$ half-width at the center of the crystal of $0.91 \pm 0.04$ mm and a divergence of $0.61 \pm 0.04$ mrad. These values agree well with $0.63 \pm 0.01$ mrad extracted from the calculations.

The data from the vertical scan at 104 cm from the crystal center are presented in Fig. 6. The results are quite different form those for the horizontal direction but may be understood phenomenologically with the aid of Fig. 7. If the plane of the down-conversion is rotated through $2\pi$ about the $z$ axis, the result is approximately a uniform ring of light for each color. A horizontal cross section through the center of the ring produces a band the width of the ring. However, this is approximately the tangent point of the ring, so a cross section in the vertical direction produces a very large band depending on the

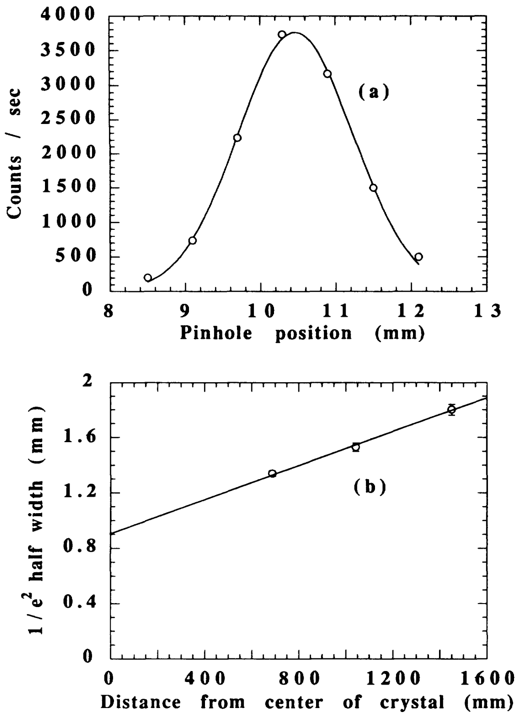

FIG. 5. An experimental single-channel measurement of the idler beam profile. (a) A sample horizontal scan measured approximately 104 cm from the center of the crystal. The solid curve is a Gaussian least squares fit. (b) The $1/e^2$ half-width as a function of distance from the crystal for evaluating divergence angle in the horizontal direction. The solid line is a linear regression.

width the ring and the width of the pinhole. Hence, the down-converted beam appears to have an oblong shape with the vertical dimension being much larger than the horizontal.

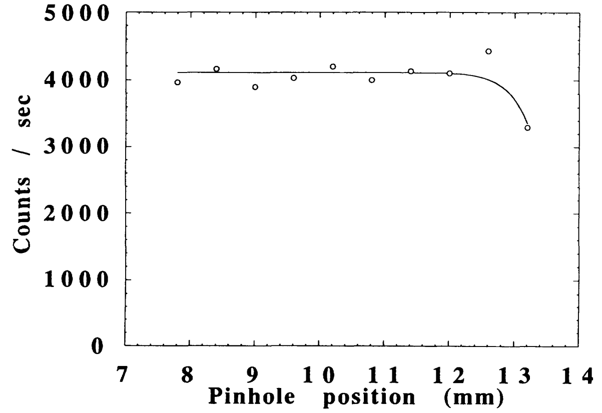

FIG. 6. A sample experimental single-channel vertical scan measured approximately 104 cm from the center of the crystal. The solid curve is a least squares fit to a rounded top-hat profile.

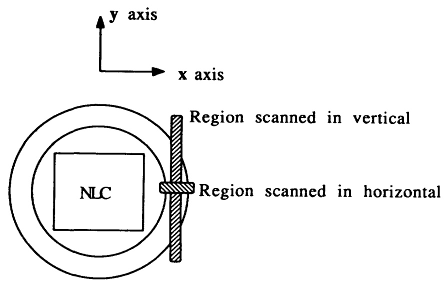

FIG. 7. A diagram demonstrating the cause of the elongation of the down-conversion in the vertical direction. The down-conversion is emitted as a cone for a particular wavelength, so a vertical scan sweeps out a large tangential portion of this cone.

The problem of coincidence counting is somewhat more complicated. From the point of view of performing calculations, the process is identical to that for single-channel measurements described above, except that now there is an independent frequency summation over each spectral function in the product, and both idler and signal angles are left to vary independently, as in Eq. (15). For each combination of $\theta_i$ and $\theta_s$, two spectral functions, $\phi(\omega_{s0}+\omega,\omega_{i0}-\omega;\omega_0|\theta_s,\theta_i;\theta_p)$ and $\phi(\omega_{s0}+\omega',\omega_{i0}-\omega';\omega_0|\theta_s,\theta_i;\theta_p)$ , are evaluated independently, and their product is summed over all values of $\omega$ and $\omega'$. In the first calculation $\theta_p = 0$, corresponding to a collimated pump, and all other parameters are the same as the single-channel calculations.

The results are shown in Fig. 8. Figure 8(a) is the angular spectrum as a function of both the signal and idler angles. As can be seen, the result is a very narrow peak at the two angles that satisfy the phase-matching conditions exactly. The measured angular spectrum of the idler beam in a coincidence measurement is determined by the geometry of the signal detection. If two pinholes are placed at fixed positions in the signal beam, as shown in Fig. 1, a detection direction and solid angle is defined. This is equivalent to averaging over a certain range of the signal angle in Fig. 8(a). If the signal pinholes define an angle in the horizontal direction of 1 mrad, centered on the optimum signal angle, the measured idler profile is given in Fig. 8(b). The result is very similar to that for the single-channel profile, with a peak centered at the same angle, but it is slightly broader with a $1/e^2$ width of $0.22 \pm 0.01$ mrad. This indicates that the coincidence profile is equivalent to the single-channel profile if the signal detector aperture is larger than the single-channel extent of the signal beam.

If we now include pump beam divergence as before by summing over the angular distribution of the pump, we obtain a much broader peak as shown in Fig. 9(a). Averaging over the signal aperture, as above, gives the effective idler profile shown as open circles in Fig. 9(b). The solid line is a least squares fit of a Gaussian with a $1/e^2$ half-width of $0.643 \pm 0.001$ mrad. Note that this is very close to the natural divergence of $0.63 \pm 0.01$ mrad for singles counts. This is reasonable since the pinhole solid angle is larger than the singles divergence spread. Therefore the singles profile, and not the fixed aperature, is the limiting dimension.

The dashed curve with solid circles in Fig. 9(b) corresponds to data from Fig. 9(a) with the averaging range for the signal shifted by half an aperture size, or 0.001 rad. The idler profile is shifted, smaller, and slightly more narrow, with a $1/e^2$ half-width of 0.546 ± 0.004 mrad. This emphasizes the substantial effect that the signal measurement has on the idler beam profile. Only the idler photons that are conjugate with detected signal photons, as determined by phase matching, can give rise to a coincidence count.

Experiments were performed as for the single-channel measurements, except that coincidence counts between signal and idler detectors were recorded as the idler pinhole was scanned with two fixed pinholes in the signal beam, defining a divergence of about 1 mrad (see Fig. 1). The results of the horizontal scan are shown in Fig. 10. Figure 10(a) is a sample beam profile at a distance of 104 cm from the center of the crystal. The width obtained by a least squares fit as a function of distance is shown in Fig. 10(b), with a divergence of 0.5 ± 0.2 mrad and a beam radius at the center of the crystal of 0.8 ± 0.3 mm. This divergence corresponds reasonably well with the value 0.643 ± 0.001 mrad obtained numerically, given the large uncertainty, but the discrepancy may indicate some off-center misalignment of the fixed signal pinhole. Since the effective aperture of the signal detector is larger than the extent of the down-conversion beam, the coincidence profile is limited by the extent of the down-conversion.

The situation is quite different for the vertical measurement. The experimental results are shown in Fig. 11. Figure 11(a) is a sample profile at a distance of 104 cm from the center of the crystal, and Fig. 11(b) is the extracted width as a function of distance. The fitted divergence and $1/e^2$ halfwidth at the crystal are 1.3 ± 0.1 mrad and 0.71 ± 0.6 mm, respectively. This is a much smaller profile than in the single-channel measurement. This is because the signal pinholes define a certain angle over which signal photons may be detected, even though there are photons emitted over a much larger region. Because of the strict correlation between signal and idler

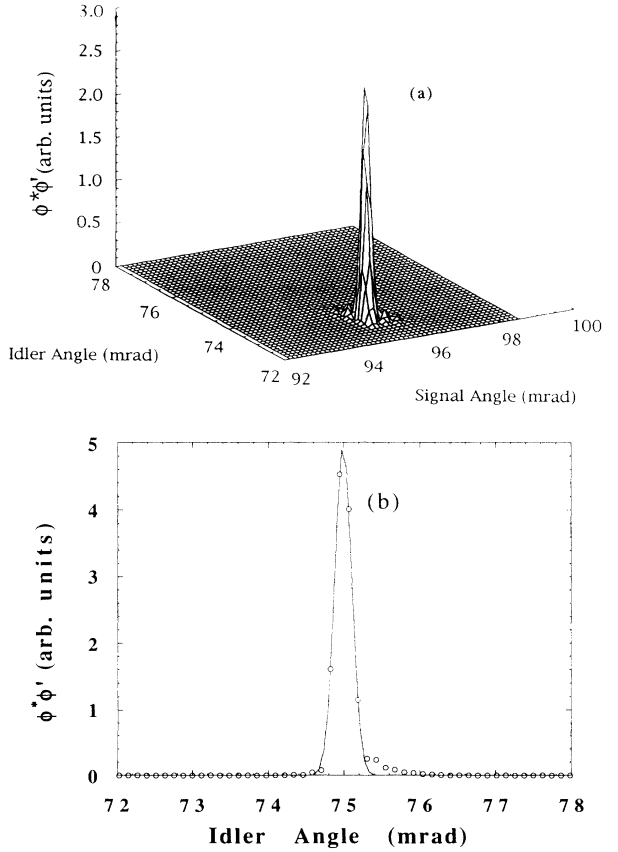

FIG. 8. (a) A numerical calculation of the combined signal and idler angular spectrum for a coincidence measurement in the case where the pump beam is perfectly collimated. (b) The profile of the conjugate portion of the idler beam in a coincidence measurement for a fixed range of signal detection. This is extracted from (a) by summing over a given range of signal angles. The solid curve is a Gaussian least squares fit.

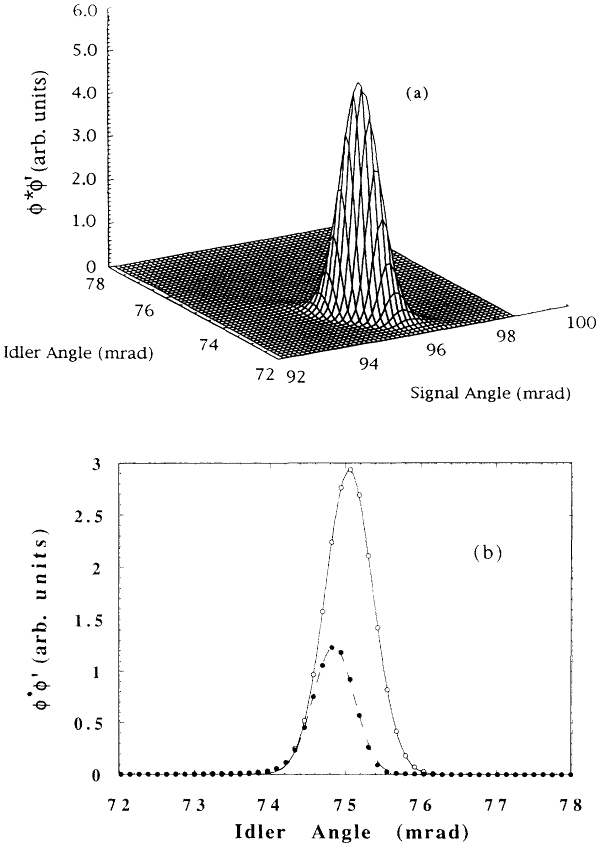

FIG. 9. (a) A numerical calculation of the combined signal and idler angular spectrum for a coincidence measurement in the case where the pump beam is divergent with a Gaussian profile. (b) The profile of the conjugate portion of the idler beam in a coincidence measurement for a fixed range of signal detection. This is extracted from (a) by summing over a given range of signal angles. The solid curve is a least squares Gaussian fit for the case where the range of signal angles is centered on the down-conversion. The dashed curve is a least squares Gaussian fit for the case when the signal range is shifted by half the width of that range.

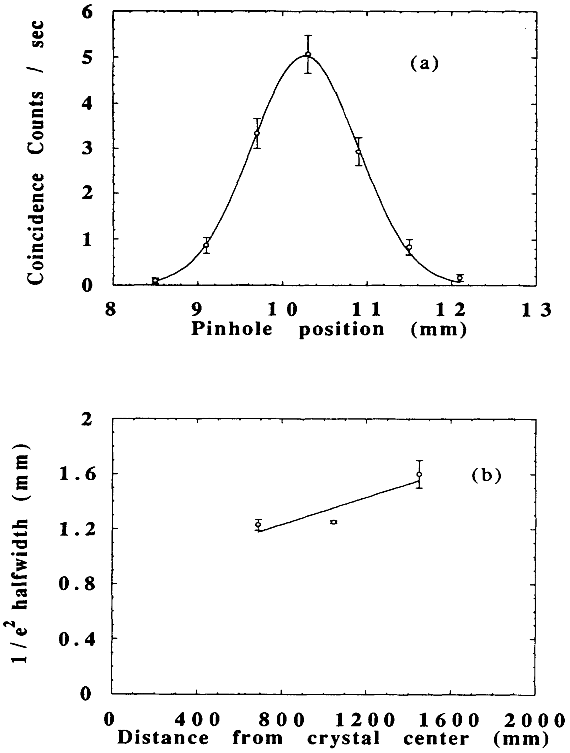

FIG. 10. An experimental coincidence measurement of the conjugate idler beam profile. (a) A sample horizontal scan measured approximately 104 cm from the center of the crystal. The solid curve is a Gaussian least squares fit. (b) The $1/e^2$ half-width as a function of distance from the crystal for evaluating divergence angle in the horizontal direction. The solid line is a linear regression.

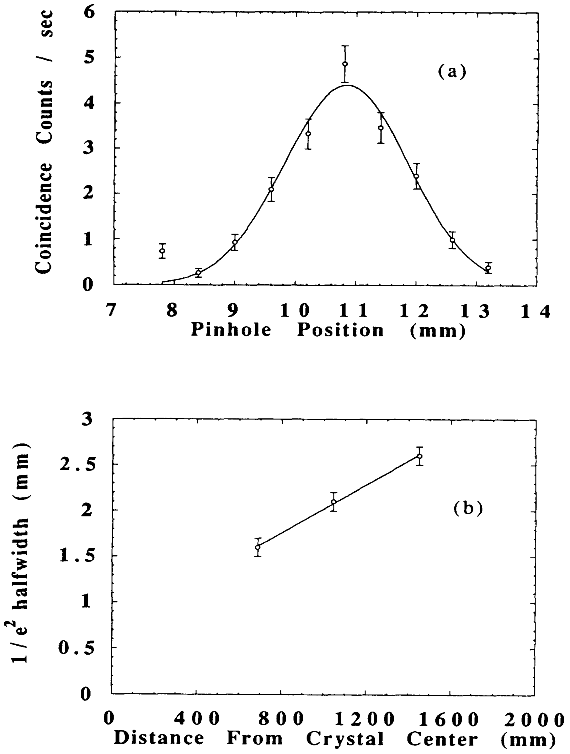

FIG. 11. An experimental coincidence measurement of the conjugate idler beam profile. (a) A sample vertical scan measured approximately 104 cm from the center of the crystal. The solid curve is a Gaussian least squares fit. (b) The $1/e^2$ half-width as a function of distance from the crystal for evaluating divergence angle in the vertical direction. The solid line is a linear regression.

photons, coincidences are only detected over the corresponding region of the idler beam. Hence the signal pinholes define the conjugate idler beam profile when they are smaller than the extent of the down-conversion. This nonlocal feature will be important in the forthcoming discussion of induced-coherence without induced emission.

## III. INDUCED COHERENCE WITHOUT INDUCED EMISSION

### A. Theory

With some basic knowledge of the spatial properties of light produced by spontaneous parametric down-conversion, it is possible to examine the effect these properties have on the process of induced emission. It is first necessary to review the induced-coherence experiment.

Induced coherence without induced emission was observed by Zou *et al.* [6]. The experimental setup is shown in Fig. 12(a). Two second-order nonlinear crystals, as described above, are pumped coherently by the same UV laser source. The signal beams are superimposed at a beam-splitter $BS_0$ to form an interferometer. One does not expect any interference between the two fields since they are products of two independent spontaneous emission processes. However, when the the idler beam from crystal 1 is carefully aligned with the idler beam from crystal 2 through crystal 2, as shown in Fig. 12(a), then interference is observed between the two signal beams at $BS_0$.

This result was analyzed theoretically by Wang *et al.* [17]. In this analysis it is noted that there is no physical interaction between the two crystals as witnessed by the fact that the average count rate of signal 2 is independent of whether or not the idler 1 connecting beam is blocked. Wang *et al.* [17] interpreted the interference as strictly due to indistinguishability of the signal paths caused by the conjugate idler photons being made indistinguishable when the beams are aligned. They derived an expression for the visibility measured by a single detector $D_s$ [17],

$$\mathcal{V} = \frac{2|\eta_1\eta_2|\sqrt{\langle I_1\rangle\langle I_2\rangle}|\gamma_{12}^{(P)}(\tau_1-\tau_2)||\tilde{\gamma}(\tau_0+\tau_2-\tau_1)|}{|\eta_1|^2\langle I_1\rangle + |\eta_2|^2\langle I_2\rangle}|\mathcal{T}|. \qquad (17)$$

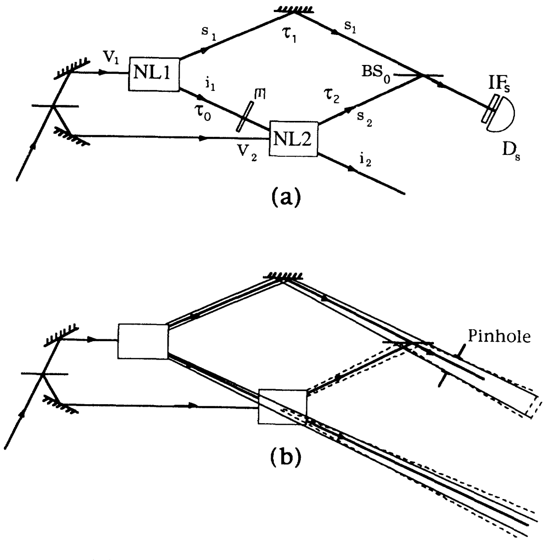

FIG. 12. (a) The experimental setup to produce induced coherence without induced emission. (b) The same experimental setup but with divergence of the fields greatly exaggerated to demonstrate the problem of spatial overlap.

Here $\langle I_1\rangle$ and $\langle I_2\rangle$ are the average pump beam intensities at crystal 1 and crystal 2, $|\eta_1|^2$ and $|\eta_2|^2$ are down-conversion efficiencies, $\gamma_{12}^{(P)}(\tau)$ is the cross-correlation function of the pump beams at the crystals, $\tilde{\gamma}(\tau)$ is the Fourier transform of the $\phi$ function given in Eq. (2) and can be thought of as the correlation function of the down-conversion, and $\mathcal{T}$ is the amplitude of the transmissivity of a beam-splitter, or in practice a neutral-density filter, placed in the idler 1 connection path. This beam-splitter has reflectivity amplitude $R$, such that $|\mathcal{T}|^2+|\mathcal{R}|^2=1$. $\tau_1$, $\tau_2$, and $\tau_0$ are optical propagation times from crystal 1 to BS$_0$, crystal 2 to BS$_0$, and crystal 1 to crystal 2, respectively.

The variation of the visibility with transmissivity $\mathcal{T}$ is another indication of the importance of indistinguishability in this process. As the transmissivity is decreased, it is more likely that a photon in the idler path after the second crystal originated in the second crystal, increasing the distinguishability of signal paths and decreasing the visibility. Another experiment was performed by Zou *et al.* [21] in which the visibility was controlled by placing various time delays in the idler path. This was interpreted in their analysis as varying the distinguishability of photon wave packets in the temporal domain. Similarly it is possible to consider variations in distinguishability in the spatial domain, which will be the main emphasis in the rest of the paper.

While the results of Zou *et al.* [6] clearly demonstrate the principle of induced coherence without induced emission in the original experiment and in all subsequent experiments utilizing the same process [21–25], the maximum visibility of the intensity modulation is less than 50%, compared to a theoretical maximum visibility of 100% when all intensities and path lengths are balanced. Furthermore, theory predicts that if $\mathcal{T}=1$, the visibilities of intensity modulation and coincidence modulation should be equal [17], but this is also not the case in practice [6].

Figure 12(b) illustrates a possible cause for this discrepancy. Figure 12(b) is identical to Fig. 12(a) except that the down-conversion beams are represented as having a finite transverse spatial dimension and divergence as discussed above. It is then apparent that even with perfectly collinear idler beams, there are some regions where it is, in principle, possible to determine if a photon originates from crystal 1 or crystal 2, so there is expected to be a corresponding decrease in the visibility.

While an exact treatment of the spatial properties of the induced-coherence process is very complicated, it is possible to perform an approximate treatment based on the analysis of Wang *et al.* [17]. The original quantum state describing the induced-coherence system is basically the sum of two single-crystal states given in Eq. (1), except that the idler 2 amplitude is replaced with a superposition of idler 1 with vacuum [17],

$$
\begin{aligned}
|\psi(t)\rangle = {} & |\mathrm{vac}\rangle_{s1,s2,i,0} + \eta_1 \frac{\delta\omega^{3/2}}{2\pi^{1/2}} \sum_{\omega_1}\sum_{\omega_1'}\sum_{\omega_1''} \phi(\omega_1',\omega_1'';\omega_1) \frac{\sin\Omega_1 t_1/2}{\Omega_1/2} e^{i\Omega_1(t-t_1/2)} v_1(\omega_1)|\omega_1'\rangle_{s1}|\mathrm{vac}\rangle_{s2}|\omega_1''\rangle_i|\mathrm{vac}\rangle_0 \\
& + \eta_2 \frac{\delta\omega^{3/2}}{2\pi^{1/2}} \sum_{\omega_2}\sum_{\omega_2'}\sum_{\omega_2''} \phi(\omega_2',\omega_2'';\omega_2) \frac{\sin\Omega_2 t_1/2}{\Omega_2/2} e^{i\Omega_2(t-t_1/2)} e^{-i(\mathbf{k}_2'+\mathbf{k}_2''-\mathbf{k}_2)\cdot\mathbf{r}_2} v_2(\omega_2)|\mathrm{vac}\rangle_{s1}|\omega_2'\rangle_{s2} \\
& \times[\mathcal{T}\,|\omega_2''\rangle_i|\mathrm{vac}\rangle_0 + \mathcal{R}\,|\mathrm{vac}\rangle_i|\omega_2''\rangle_0]\ . \qquad (18)
\end{aligned}
$$

It must be noted that in the derivation of this equation, the one-photon Fock states $|\omega\rangle_j$ are originally dependent not just on frequency but rather on wave vector and polarization. The transformation to frequency is made by assuming fixed directions and polarizations, so the wave vector is then solely dependent on frequency.

To retain information about divergence of the fields, one can proceed in a manner similar to that above for a single crystal. If the wave vectors are decomposed in two dimensions, $\mathbf{k}_j = k_j\sin(\theta_j)\mathbf{x} + k_j\cos(\theta_j)\mathbf{z}$, where $k_j = n_j(\omega_j)\omega_j/c$, the sum over wave vectors may be replaced with a double sum over frequency and angle.

Applying this decomposition modifies Eq. (18) to give

$$
\begin{aligned}
|\psi(t)\rangle = {} & |\mathrm{vac}\rangle_{s1,s2,i,0} + \eta_1 \frac{\delta\omega^3}{2\pi^{1/2}} \sum_{\omega_1}\sum_{\omega_1'}\sum_{\omega_1''}\sum_{\theta_1}\sum_{\theta_1'}\sum_{\theta_1''} \phi(\omega_1',\omega_1'';\omega_1|\theta_1',\theta_1'';\theta_1) \frac{\sin\Omega_1 t_1/2}{\Omega_1/2} e^{i\Omega_1(t-t_1/2)} \\
& \times v_1(\omega_1,\theta_1)|\omega_1',\theta_1'\rangle_{s1}|\mathrm{vac}\rangle_{s2}|\omega_1'',\theta_1''\rangle_i|\mathrm{vac}\rangle_0 \\
& + \eta_2 \frac{\delta\omega^3}{2\pi^{1/2}} \sum_{\omega_2}\sum_{\omega_2'}\sum_{\omega_2''}\sum_{\theta_2}\sum_{\theta_2'}\sum_{\theta_2''} \phi(\omega_2',\omega_2'';\omega_2|\theta_2',\theta_2'';\theta_2) \frac{\sin\Omega_2 t_1/2}{\Omega_2/2} e^{i\Omega_2(t-t_1/2)} \\
& \times e^{-i(\mathbf{k}_2'+\mathbf{k}_2''-\mathbf{k}_2)\cdot\mathbf{r}_2} v_2(\omega_2,\theta_2)|\mathrm{vac}\rangle_{s1}|\omega_2',\theta_2'\rangle_{s2}[\mathcal{T}\,|\omega_2'',\theta_2''\rangle_i|\mathrm{vac}\rangle_0 + \mathcal{R}\,|\mathrm{vac}\rangle_i|\omega_2'',\theta_2''\rangle_0] \,. \qquad (19)
\end{aligned}
$$

Here the $\phi$ functions of Eq. (18) are replaced with the angle-dependent $\phi$ functions given in Eq. (6), and the Fock states are made dependent upon angle as well as frequency, with different angular modes orthogonal,

$$\langle\omega_{i'},\theta_{j'}|\omega_i,\theta_j\rangle = \delta_{i,i'}\delta_{j,j'}.$$

First the single-channel counting rate at detector $D_s$ will be evaluated. To include the effect of angular spread, the field operator can be written as

$$\hat{E}_j^{(+)}(\mathbf{r},t) = \left(\frac{\delta\omega}{2\pi}\right)^{1/2} \sum_{\omega_j}\sum_{\theta_j} g_j(\theta_j)\hat{a}_j(\omega_j,\theta_j)e^{-i\omega_j t}, \qquad (20)$$

where $g_j(\theta)$ is the angular acceptance spectrum of the detector for the field $j$. Assuming $\mathrm{BS}_0$ is 50%-50% and symmetric, the field at detector $D_s$ is then given by

$$\hat{E}_s^{(+)}(\mathbf{r},t) = \frac{1}{\sqrt{2}}[\hat{E}_{s1}^{(+)}(\mathbf{r},t-\tau_1) + i\hat{E}_{s2}^{(+)}(\mathbf{r},t-\tau_2)]. \qquad (21)$$

The signal photon count rate is calculated from

$$R_s = \alpha_s \langle\psi|\hat{E}_s^{(-)}(\mathbf{r},t)\hat{E}_s^{(+)}(\mathbf{r},t)|\psi\rangle, \qquad (22)$$

where $\alpha_s$ is the quantum efficiency of the signal detector $D_s$. When the field given in Eq. (21) is used with the state vector of Eq. (19) in the expression for counting rate, Eq. (22), after some algebra there appear terms like

$$
\begin{aligned}
(\delta\omega)^3 \sum_{\omega_1}\sum_{\omega_2}\sum_{\omega}\sum_{\theta}\sum_{\theta_1}\sum_{\theta_1'}\sum_{\theta_2}\sum_{\theta_2'} & g_{s1}^*(\theta_1')g_{s2}(\theta_2')\phi_1^*(\omega_0-\omega,\omega;\omega_0|\theta_1',\theta;\theta_1)\phi_2(\omega_0-\omega,\omega;\omega_0|\theta_2',\theta;\theta_2) \\
& \times e^{-i\omega_2(t-\tau_2)}e^{i\omega_1(t-\tau_1)}e^{-i\omega(\tau_2+\tau_0-\tau_1)}\, v_1^*(\omega_1,\theta_1)v_2(\omega_2,\theta_2). \qquad (23)
\end{aligned}
$$

The pump field amplitude is factorized as $v_j(\omega,\theta) = \tilde{v}_j(\omega)g_{pj}(\theta)$, where $\tilde{v}_j(\omega)$ is the amplitude of the $\omega$ Fourier component of pump field $j$, and $g_{pj}(\theta)$ is the angular spectrum of pump beam $j$. Also we assume that the $\phi$ function may be factorized as

$$\phi_j(\omega_0-\omega,\omega;\omega_0|\theta_j',\theta;\theta_j) = \tilde{\phi}(\omega_0-\omega,\omega;\omega_0)f_j(\theta_j',\theta;\theta_j),$$

where $\tilde{\phi}(\omega_0-\omega,\omega;\omega_0)$ is the original spectral function of the down-conversion given in Eq. (2), and $f_j(\theta_j',\theta;\theta_j)$ is an angular spectral function representing the phase matching of crystal $j$. This assumption is the weakest part of the calculation, since this factorization is not obviously true in all situations, and much care must be given to the interpretation of the resulting $f$ function.

If such factorizations are valid, the resulting count rate is then very similar to that obtained by Wang *et al.* [17],

$$R_s = \frac{\alpha_s}{2}[|\eta_1|^2\langle I_1\rangle\mathcal{G}_{11} + |\eta_2|^2\langle I_2\rangle\mathcal{G}_{22} + i\eta_1^*\eta_2\gamma_{12}(\tau_1-\tau_2)\tilde{\gamma}(\tau_2+\tau_0-\tau_1)\sqrt{\langle I_1\rangle\langle I_2\rangle}\mathcal{G}_{12}e^{-i\omega_{i0}(\tau_2+\tau_0-\tau_1)} + \text{c.c.}], \qquad (24)$$

where

$$\mathcal{G}_{ij} \equiv \sum_{\theta}\left[\sum_{\theta_i}\sum_{\theta_i'} g_{si}^*(\theta_i')g_{pi}^*(\theta_i)f_i^*(\theta_i',\theta;\theta_i)\right]\left[\sum_{\theta_j}\sum_{\theta_j'} g_{sj}(\theta_j')g_{pj}(\theta_j)f_j(\theta_j',\theta;\theta_j)\right]. \qquad (25)$$

This function represents the geometric collection efficiency of the detector and also, when $i \neq j$, the degree of idler beam overlap. This may be understood by examining the funtion $f_j(\theta_j',\theta;\theta_j)$. This function describes the distribution of signal and idler angles for a given pump beam angular distribution, as discussed above. By summing over the signal and pump angles with weightings defined by experimental parameters, we find that there is now a well-defined conjugate idler distribution as well. When $i \neq j$, summing over the idler angle makes the magnitude of $\mathcal{G}_{ij}$ proportional to the degree of overlap.

The count rate above results in a second-order visibility of

$$\mathcal{V}^{(2)} = \frac{2|\eta_1\eta_2|\sqrt{\langle I_1\rangle\langle I_2\rangle}\,|\gamma_{12}(\tau_1-\tau_2)||\tilde{\gamma}(\tau_2+\tau_o-\tau_1)||\mathcal{G}_{12}|}{|\eta_1|^2\langle I_1\rangle\mathcal{G}_{11} \;+\; |\eta_2|^2\langle I_2\rangle\mathcal{G}_{22}}|\mathcal{T}|. \tag{26}$$

If all intensities and conversion efficiencies are equal, $|\eta_1|^2 = |\eta_2|^2$ and $\langle I_1\rangle = \langle I_2\rangle$, and there are no losses in the idler connection, $|\mathcal{T}| = 1$, then

$$\mathcal{V}^{(2)} = \frac{2|\mathcal{G}_{12}|}{\mathcal{G}_{11} \;+\; \mathcal{G}_{22}}.$$

If the collection efficiencies are identical for each detector, and the idlers overlap exactly at all points after crystal 2, then $\mathcal{G}_{11} = \mathcal{G}_{22} = \mathcal{G}_{12}$, and the visibility achieves a maximum value of unity. It is, in principle, possible to balance the collection efficiencies, or at least to compensate by adjusting the respective pump beam intensity. However, except for the ideal case of perfectly collimated idler beams, the overlap will never be exact, and the second-order visibility will never be unity.

It is a fairly straightforward extension to repeat this calculation for the case of the coincidence counting rate between the signal detector $D_s$ and a similar detector in the idler beam $D_i$. The coincidence counting rate is given by

$$R_{s,i} = \int_{-T_c/2}^{T_c/2} d\tau\,\alpha_s\alpha_i\,\langle\psi|\hat{E}_s^{(-)}(\mathbf{r},t)\hat{E}_i^{(-)}(\mathbf{r},t+\tau)\hat{E}_i^{(+)}(\mathbf{r},t+\tau)\hat{E}_s^{(+)}(\mathbf{r},t)|\psi\rangle,$$

where the field operators have the same form as given in Eq. (20), $\alpha_i$ is the quantum effieciency of detector $D_i$, and $T_c$ is the coincidence counting time.

Evaluation of this expression with the quantum state given in Eq. (19) gives the following result:

$$R_{s,i} = \frac{\alpha_s\alpha_i}{2}\,[|\eta_1|^2\langle I_1\rangle\tilde{\mathcal{G}}_{11}|\mathcal{T}|^2 \;+\; |\eta_2|^2\langle I_2\rangle\tilde{\mathcal{G}}_{22} + i\eta_1^*\eta_2\gamma_{12}(\tau_1-\tau_2)\tilde{\gamma}(\tau_2+\tau_0-\tau_1)\sqrt{\langle I_1\rangle\langle I_2\rangle}\tilde{\mathcal{G}}_{12}e^{-i\omega_{i0}(\tau_2+\tau_0-\tau_1)} \;+\; \text{c.c.}], \tag{27}$$

where $\tilde{\mathcal{G}}_{ij}$ is similar to the function $\mathcal{G}_{ij}$ given in Eq. (25), except that now the two idler angles are summed independently, weighted by the respective idler detector acceptance angle distributions,

$$\tilde{\mathcal{G}}_{lm} \equiv \left[\sum_{\theta_l}\sum_{\theta_l'}\sum_{\theta_l''} g_{il}^*(\theta_l'')g_{sl}^*(\theta_l')g_{pl}^*(\theta_l)f_l^*(\theta_i',\theta_l'';\theta_l)\right]\left[\sum_{\theta_m}\sum_{\theta_m'}\sum_{\theta_m''} g_{im}(\theta_m'')g_{sm}(\theta_m')g_{pm}(\theta_m)f_m(\theta_m',\theta_m'';\theta_m)\right]. \tag{28}$$

This function may again be interpreted as a measure of the collection efficiency and of the idler overlap, but now the idler overlap is due to the overlap of the idependent idler angular spectrum of each crystal with the detector aperture acceptance angle.

The fourth-order visibility is then

$$\mathcal{V}^{(4)} = \frac{2|\eta_1\eta_2|\sqrt{\langle I_1\rangle\langle I_2\rangle}\,|\gamma_{12}(\tau_1-\tau_2)||\tilde{\gamma}(\tau_2+\tau_o-\tau_1)||\tilde{\mathcal{G}}_{12}|}{|\eta_1|^2\langle I_1\rangle\tilde{\mathcal{G}}_{11}|\mathcal{T}|^2 \;+\; |\eta_2|^2\langle I_2\rangle\tilde{\mathcal{G}}_{22}}|\mathcal{T}|. \tag{29}$$

If again all intensities and conversion efficiencies are balanced, and the idler connection transmissivity is unity, the visibility is

$$\mathcal{V}^{(4)} = \frac{2|\tilde{\mathcal{G}}_{12}|}{\tilde{\mathcal{G}}_{11} \;+\; \tilde{\mathcal{G}}_{22}}.$$

To satisfy the condition that $\tilde{\mathcal{G}}_{11} = \tilde{\mathcal{G}}_{22} = \tilde{\mathcal{G}}_{12}$, and therefore to achieve unity visibility, the collection efficiencies must again be the same for all four beams, but now the two idler beams need only overlap within the idler detector aperture. In other words, for the case of fourth-order interference, the idler photons need not be intrinsically indistinguishable, but only indistinguishable within the accuracy of detection, whereas for second-order interference the idler beams must be intrinsically indistinguishable. This conclusion is qualitatively consistent with the results of Zou *et al.* [6].

### B. Experimental results

It is possible to test the foregoing theoretical conclusions by producing induced coherence and measuring the second- and fourth-order visibilities and then measuring the angular spectra of the idler conjugates for each crystal. The overlap functions $\mathcal{G}_{12}$ and $\tilde{\mathcal{G}}_{12}$ may be evaluated from the conjugate idler angular spectra, and the functions $\mathcal{G}_{11}$, $\mathcal{G}_{22}$, $\tilde{\mathcal{G}}_{11}$, and $\tilde{\mathcal{G}}_{22}$ may be evaluated approximately just from the geometry of the setup.

The experimental setup is shown in Fig. 12. Two 1.0 mm diameter pinholes are placed in the signal beam at distances 30 cm and 90 cm after the beam-splitter $BS_0$, and then define the signal detection acceptance profile. A single 3 mm diameter pinhole is placed in front of the idler detector at a distance of approximately 75 cm from the center of the second crystal. The idler 1 connection and the interferometer are aligned to give the best possible visibility, measured by translating beam-splitter $BS_0$ through small distances with a piezo transducer and recording the count rates of the signal detector $D_s$ and the coincidence counter between detectors $D_s$ and $D_i$. The results of the visibility measurements are shown in Fig. 13, with Fig. 13(a) corresponding to second-order interference and Fig. 13(b) to fourth-order interference. A sinusoidal modulation is fit to each set of data by a least squares fitting routine, giving visibilities of $0.49 \pm 0.03$ for second-order interference and $0.76 \pm 0.07$ for fourth-order interference.

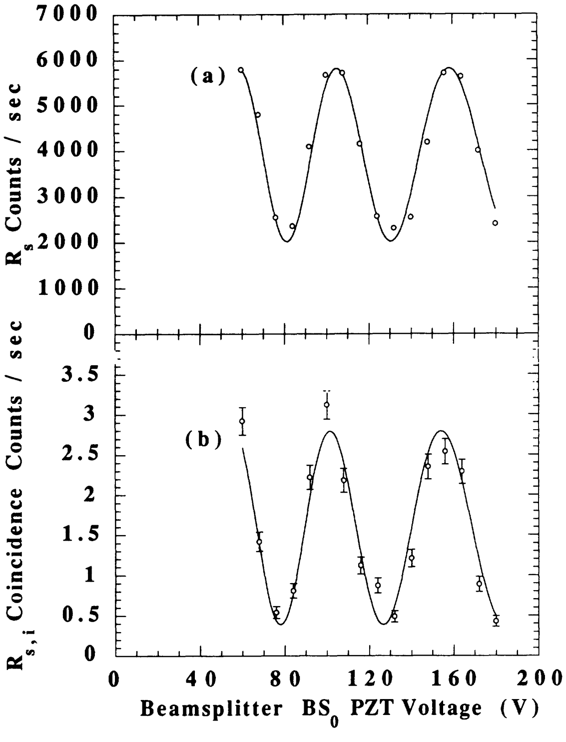

FIG. 13. Experimental visibility measurements showing counting rates as a function of the position of beam-splitter $BS_0$ controlled by a piezoelectric translator. (a) Single-channel measurement showing counting rate of detector $D_s$. (b) Coincidence measurement showing coincidence counting rate between detectors $D_s$ and $D_i$. The solid curves in each are least squares fits to an offset sine function. The amplitude and visibility were left as free parameters, while the period was fixed. The phase was fit as free parameter for the single-channel data but was then fixed to that value for the coincidence data.

The conjugate idler beam profiles were measured by replacing the 3 mm pinhole in front of the idler detector, with the 600 $\mu$m used for the profile measurements above. The pinhole was scanned in both the horizontal and vertical directions while recording the coincidence count rate. Then the detector and pinhole were moved to various distances from the second crystal, and the procedure was repeated. The results of a sample scan at a distance of 75 cm from the center of crystal 2 are shown in Fig. 14. Figure 14(a) gives the horizontal scan, and Fig. 14(b) the vertical scan. In both figures the solid circles with the dashed line are data taken from crystal 1, and the open circles with the solid line are data from crystal 2.

In principle, angular spectra for each crystal can be extracted from these data and the geometrical factors $\mathcal{G}_{ij}$ may be evaluated. However, in practice this is not possible, due to the oversimplification of the theoretical model, which relies only on angular distributions. There is also an experimental problem.

Using only angular spectra in the theoretical calulation implies that the two pairs of beams have a common origin. The theory can handle longitudinal separations of the origins by appropriate modification of the aperture

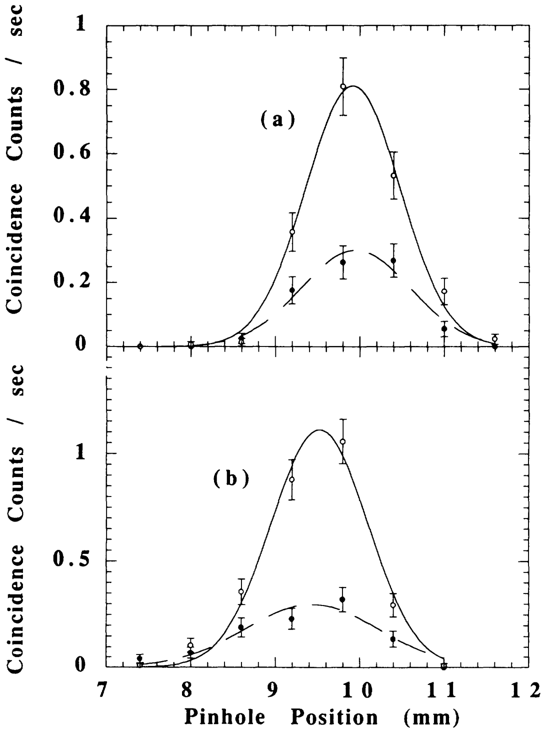

FIG. 14. Sample coincidence scans of conjugate idler beams in (a) the horizontal direction and (b) the vertical direction, showing overlap. The solid curves with open circles are for crystal 2 idler and the dashed curves with solid circles are for crystal 1 idler. The curves are Gaussian least squares fits.

acceptance angles. But lateral shifts of origin, resulting from misalignment, cannot be treated within the framework of the current model.

The experimental limitation involves the alignment of pinholes defining the signal beams. If these pinholes are not carefully centered on the down-conversion, the resulting conjugate idler profile may be diminished, as was demonstrated in the numerical calculations of the section above [see the dashed curve of Fig. 9(b)]. If there is an additional misalignment, so that the pinholes are shifted as well as being at a wrong angle, this effect becomes worse as measurements are made farther from the crystal, as depicted in Fig. 15. Thus, the measured idler coincidence profile appears to diverge and then converge again, making it impossible to extract an angular spectrum.

Despite the breakdown of the theoretical model, it is possible to make some rough numerical estimates of the idler overlap by extrapolating the idler beam profiles back to the center of crystal 2 and calculating a percentage overlap of areas. The profile data gives idler 1 a larger cross section but a smaller divergence angle at crystal 2 than for idler 2. The extrapolated areas of the idler 1 and 2 beams at the center of crystal 2 are 6.5 mm and 4.2 mm, respectively, giving a relative overlap of 45%. If this is interpreted as the degree of indistinguishability, giving a rough estimate of visibility, this compares reasonably well with the measured visibility of 49%.

The above analysis also provides a qualitative explanation for the discrepancy between second- and fourth-order visibility, even though a quantative comparison cannot be achieved without obtaining a good angular spectrum for the idler coincidence. The functions $\tilde{\mathcal{G}}_{ij}$ defined in Eq. (28) are based upon idependent summations of each idler coincidence spectrum multiplied by the acceptance spectrum of the detector. In the experiment the aperture of the idler detector was about 3 mm, compared to the $1/e^2$ full width of the idler beams at the position of the detector of about 3.2 mm. Therfore a majority of the two beams was collected, resulting in higher visibility than for the second order.

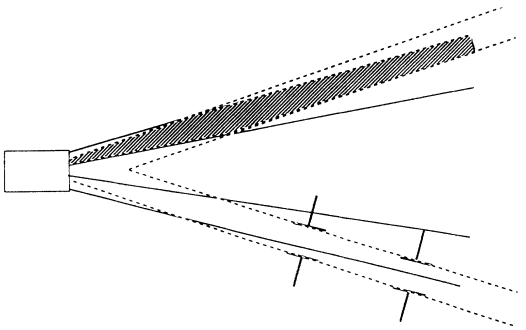

FIG. 15. Diagram illustrating how misalignment of signal pinholes may clip the conjugate idler as measurements are taken farther from the crystal, causing the conjugate idler to appear to diverge until a certain distance and then converge after that point. The solid lines represent the extent of the down-conversion beams, the dashed lines represent the beam defined by the pinholes and the corresponding conjugate idler path, and the shaded region is the conjugate idler actually detected.

Since measurement of the idlers is made, the two idler photons need only be indistinguishable to within the resolution of the detector, as opposed to being intrinsically indistinguishable as for second-order interference. An extreme case of this situation has already been demonstrated in a previous experiment that also utilized two down-converters, but where the idler beams only overlapped at a beam splitter and nowhere else [3]. In this case no second-order interference was observed, but there was fourth-order interference.

## IV. SUMMARY AND CONCLUSIONS

A theoretical model to describe the spatial properties of spontaneous parametric down-conversion has been derived. Numerical calculations of beam profiles for both single-channel and coincidence measurements based upon this model gave results in good agreement with measurements. It was found that, for these working parameters, the divergence of the pump beam has a greater influence on the spatial properties of the down-conversion than the effects of frequency selection and phase matching. Also, the strong nonlocal correlation between signal and idler was demonstrated in the numerical calculations by showing what effect moving pinholes in the signal beam has on the coincidence profile of the idler beam and was shown experimentally by the clipping of the vertical single-channel distribution.

This three-dimensional model was then applied to the phenomenon of induced coherence without induced emission. This model predicts that visibility is reduced by spatial nonoverlap resulting from the divergence properties of the down-conversion, even for perfect alignments. It also predicts that it may be easier to achieve higher visibility in fourth-order interference than in second order, While the experimental results did not provide precise confirmation of the theory, they were consistent with the spirit of the theory.

The results of this experiment suggest ways in which the visibility of the induced coherence may be improved. For fourth-order measurements the visibility can in principle be increased to near 100% simply be enlarging the detector aperture. Of course there are practical limitations to improved visibility, since a larger aperture also increases background light which decreases visibility.

For second-order measurements improvement depends on ways of matching the spatial profiles of the two down-conversions. For the layout shown in Fig. 12, idler 1 is always less divergent and wider at crystal 2 than idler 2, because of the requirement for balancing the path length of signal 1 against the combined path lengths of signal 2 and the idler 1 connection, i.e., $\tau_1 - \tau_2 - \tau_0 \ll T_{\rm DC}$. One obvious way to make the two signal paths of the same length, and therefore achieve similar beam divergence, would be to make the coherence length longer than the idler 1 connection length. But this is not practical, as it would reduce the counting rate below the level of detectablility. Another possibility would be to place an aperture in the signal 1 arm of the interferometer to define the same divergence angle for signal 1 as for signal 2, and to place an aperture in the pump beam 1 so that the size of the two idlers is the same at the center of crystal 2. This would be a difficult procedure and would require careful balancing of the pump intensities to allow for loss of down-conversion from crystal 1 at the apertures. Perhaps the most practical, but also least effective, way to improve second-order visibility is simply to make the idler 1 connection as short as possible. This limits the difference between the signal path lengths, and hence the difference in divergences, and also minimizes the size difference of the two idlers at the center of crystal 2.

Finally the prediction and explaination of the discrepancy between fourth- and second-order visibilities, emphasizes the distinction between intrinsic and nonintrinsic indistinguishability and the role that distinciton plays in quantum interference. When an observer actively makes a measurement in an attempt to distinguish possible paths, such as the idler measurement in the case of coincidence measurement, the possible paths need only be indistinguishable within the resolution of the detection system. On the contrary when no auxiliary observation is made, whether or not any interference is observed then depends solely upon intrinsic indistinguishability. The latter case seems to imply that there is some type of collapse of the quantum state independent of any observations.

## ACKNOWLEDGMENTS

The authors are indebted to Dr. Leonard Mandel, Department of Physics and Astronomy, University of Rochester, for many useful discussions about this work and for proofreading the manuscript. This work was supported by the National Science Foundation and by the U.S. Office of Naval Research. One of us (G.A.B.) would also like to acknowledge the support of CNPq (Conselho Nacional de Desenvolvimento Científico e Tecnológico, Brazil).

---

[1] Z. Y. Ou and L. Mandel, Phys. Rev. Lett. **61**, 50 (1988).
[2] Z. Y. Ou and L. Mandel, Phys. Rev. Lett. **62**, 2941 (1989).
[3] Z. Y. Ou, L. J. Wang, and L. Mandel, Phys. Rev. A **40**, 1428 (1989).
[4] R. A. Campos, B. E. A. Saleh, and M. C. Teich, Phys. Rev. A **42**, 4127 (1990).
[5] X. Y. Zou, L. J. Wang, and L. Mandel, Opt. Commun. **84**, 351 (1991).
[6] X. Y. Zou, L. J. Wang, and L. Mandel, Phys. Rev. Lett. **67**, 318 (1991).
[7] G. A. Barbosa and C. Henrique Monken, Phys. Rev. Lett. **67**, 3372 (1991).
[8] P. G. Kwiat, A. M. Steinberg, and R. Y. Chiao, Phys. Rev. A **45**, 7729 (1992).
[9] A. M. Steinberg, P. G. Kwiat, and R. Y. Chiao, Phys. Rev. Lett. **68**, 2421 (1992).
[10] M. Belsley, O. T. Smithey, M. G. Raymer, and J. Mostowski, Phys. Rev. A **46**, 414 (1992).
[11] T. G. Giallorenzi and C. L. Tang, Phys. Rev. **166**, 225 (1968).
[12] S. K. Wong, G. Fournier, P. Mathieu, and P. Pace, J. Appl. Phys. **71**, 1091 (1992).
[13] G. C. Bhar and U. Chatterjee, Jpn. J. Appl. Phys. **29**, 1103 (1990).
[14] B. Huttner, S. Serulnik, and Y. Ben-Aryeh, Phys. Rev. A **42**, 5594 (1990).
[15] Karl Koch, E. C. Cheung, Gerald T. Moore, Stephen H. Chakmakjian, and J. M. Liu, IEEE Trans. Quantum Electron. (to be published).
[16] L. J. Wang, doctoral thesis, Department of Physics and Astronomy, University of Rochester (1992) (unpublished).
[17] L. J. Wang, X. Y. Zou, and L. Mandel, Phys. Rev. A **44**, 4614 (1991).
[18] L. Mandel, Opt. Commun. **16**, 1882 (1991).
[19] M. Born and E. Wolf, *Principles of Optics*, 6th ed. (Pergamon, Oxford, 1980).
[20] *Handbook of Laser Science and Technology* (CRC Press, Boca Raton, FL, 1986), Vol. III, p. 108.
[21] X. Y. Zou, T. P. Grayson, G. A. Barbosa, and L. Mandel, Phys. Rev. A **47**, 2293 (1993).
[22] X. Y. Zou, T. P. Grayson, L. J. Wang, and L. Mandel, Phys. Rev. Lett. **68**, 3667 (1992).
[23] X. Y. Zou, T. P. Grayson, and L. Mandel, Phys. Rev. Lett. **69**, 3041 (1992).
[24] T. P. Grayson, X. Y. Zou, D. Branning, J. R. Torgerson, and L. Mandel, Phys. Rev. A **48**, 4793 (1993).
[25] T. P. Grayson, J. R. Torgerson, and G. A. Barbosa, Phys. Rev. A **49**, 626 (1994).